INTERNATIONAL JOURNAL OF Telecommunications
AIR DEFENSE COLLEGE

Leveraging Nature-Inspired Search to Boost CNN Performance in Colorectal Cancer Classification

Citation: Mohammed, I.; Bakr, N, Moustafa, H., Moustafa, A., Amer, H.
Inter. Jour. of Telecommunications, ***IJT'2025****, Vol. 05, Issue 02, pp. 1-20, 2025.*
Doi: 10.21608/ijt.2025.411907.1130
Editor-in-Chief: Youssef Fayed.
Received: 07/08/2025.
Accepted date: 12/09/2025.
Published date: 12/09/2025.

Islam A. A. Mohammed[1*], Nour S. Bakr[2], Hossam Moustafa[3], Adel F. Mohamed Moustafa[4], Hanan M. Amer[5].
*[1]Program of Medical and Biological Engineering, Faculty of Engineering, Mansoura University, Mansoura, Egypt. islamaamohammed@hti.ed.eg
[2]Biomedical Engineering Department, Higher Technological Institute, 10th of Ramadan City, El Sharkia, Egypt. nour.bakr@hti.edu.eg
[3]Department of Electronics and Communications Engineering at the Faculty of Engineering, Mansoura Uni-versity, Mansoura, Egypt. hossam_moustafa@mans.edu.eg
[4]Oncology Center, Mansoura University, Mansoura, Egypt. dr_adel_fathe@mans.edu.eg.
[5] Electronics and Communications Engineering Department, Faculty of Engineering, Mansoura University, Mansoura, Egypt. Faculty of Engineering, Mansoura National University, Mansoura, Egypt.
eng_hanan_2007@mans.edu.eg.

Abstract: Cancer affecting the colorectal region (CRC) is a leading contributor to worldwide cancer-associated mortality, where timely and precise diagnosis is critical for enhancing patient prognosis. Although histopathology remains the benchmark for diagnostic accuracy, its manual assessment is time-consuming and subject to variability among pathologists. To address these challenges, this paper proposes a novel optimization framework "CrcMRFA," based on the Manta Ray Foraging Optimization (MRFO) algorithm to fine-tune convolutional neural nets initialized with learned weights from prior training for histopathological image classification. Three architectures-VGG16, ResNet50, and DenseNet121 were optimized with respect to key hyperparameters, encompassing parameters such as learning rate, batch size, dropout rate, and the number of trainable layers. Experimental evaluation leveraging the Kather_texture_2016_image_tiles_5000 dataset demonstrated significant performance enhancements across all metrics. The optimized ResNet50 achieved the best results, with accuracy improving from 90.32% to 95.97% and the Weighted Sum Metric (WSM) exceeding 96.77%. These findings highlight the potential of MRFO in automating CNN optimization for robust and efficient CRC tissue classification.

Keywords: Histopathological; Colorectal Cancer (CRC); Convolutional Neural Network (CNN); Manta Ray Foraging Optimization (MRFO); Transfer Learning (TL).

1. Introduction

Cancer involves the abnormal and uncontrolled proliferation of cells, which can infiltrate and harm nearby tissues [1]. Colorectal cancer (CRC), often known as colon cancer, originates in the colon a 1.5-meter-long muscular component of the digestive system. Many of these cancers begin as noncancerous adenomatous polyps in the colon lining, which can progress to malignancy if not detected and removed [2].

As of 2020, CRC has emerged as the third most common cancer on a worldwide scale, with around 1.93 million newly diagnosed cases, and was the second leading cause of cancer-related mortality, accounting for close to one million deaths [3]. Projections indicate that by 2040, the number of new CRC cases everywhere will rise to 3.2 million [4].

CRC can be identified using both indirect methods, such as blood tests assessing liver and kidney function, and direct visualization techniques, including colonoscopy and computed tomography (CT) scans. Despite the availability of these tools, histopathological examination of tissue biopsies remains the definitive diagnostic method. [5]. This process involves pathologists inspecting tissue samples under a microscope to evaluate cellular architecture, morphology, and detect potential anomalies [6]. However, such manual evaluations are often labor-intensive, expensive, and subject to individual interpretation, depending significantly on the pathologist's experience. [7]. Consequently, the reliance on automated diagnostic systems is rising, driven by the need for speed, consistency, and objectivity in medical assessments [8].

Recent progress in artificial intelligence (AI) has enabled the development of deep learning (DL) techniques, particularly Convolutional Neural Networks (CNNs), that have shown superior performance in the analysis of medical images [9]. CNNs are especially effective for tasks involving feature extraction and image classification [10]. Their applications cover various areas of medical imaging, such as detecting skin cancer [11], identifying lung and brain tumors [12], diagnosing liver conditions [13], and recognizing breast cancer [14]. Additionally, CNNs have proven to be highly accurate in classifying colorectal cancer (CRC) histopathological images, often requiring minimal preprocessing [15].

Enhancing the performance of such models often relies on optimization strategies. Metaheuristic algorithms are particularly favored due to their flexibility and efficiency in fine-tuning model parameters [16]. Prominent examples of these algorithms include the Grasshopper Optimization Algorithm (GOA) [17], Owl Search Algorithm (OSA) [18], Cuckoo Search (CS) [19], Whale Optimization Algorithm (MOA) [20], gorilla troops optimization algorithm (GTO) [21], and Mayfly Optimization Algorithm (MOA) [22].

Among various optimization methods, Manta Ray Foraging Optimization (MRFO) [23] distinguishes itself through its unique chain, cyclone, and somersault foraging mechanisms, which provide a dynamic and adaptive balance between exploration and exploitation. Unlike Particle Swarm Optimization (PSO), which may prematurely converge due to limited diversity in the swarm, or Genetic Algorithms (GA), which often require extensive parameter tuning and incur higher computational cost, MRFO introduces flexible search phases that maintain population diversity while steadily guiding solutions toward optimal regions. This dynamic behavior enables MRFO to avoid stagnation at a local minimum, a common challenge in high-dimensional search spaces. Such characteristics are particularly advantageous for convolutional neural network (CNN) hyperparameter optimization in medical imaging, where the parameter space is complex, non-convex, and prone to overfitting. By leveraging its adaptive exploration–exploitation trade-off, MRFO facilitates more efficient identification of robust hyperparameter configurations, making it especially suitable for applications such as [24], [25].

Primary Contributions to this Study

- **Establishment of Baseline Metrics:** Pre-trained CNN models are assessed using the *Kather_texture_2016_image_tiles_5000* dataset to provide a reference for performance comparison.
- **MRFO-Based Hyperparameter Optimization:** Critical training parameters—including optimizer choice, batch size, layer freezing configuration, and dropout rate—are adaptively optimized via MRFO for three popular pre-trained architectures.
- **Efficiency Analysis:** The study assesses the influence of MRFO on training efficiency, considering convergence validation accuracy.
- **Comparative Benchmarking:** The proposed MRFO-enhanced approach is benchmarked against contemporary methods to underscore its performance gains in accuracy and computational efficiency.

The rest of this paper is organized as follows: Section 2 explains relevant research on colorectal cancer image classification. Section 3 provides an in-depth exposition of the adopted methodology. Behind the CrcMRFA architecture and its components. Section 4 details results and comparative analysis. Section 5 concludes the study and proposes directions for future work.

2. **Related Work**

Recent advances in colorectal cancer (CRC) histopathology classification have explored a variety of strategies.

One of the first examples of applying convolutional neural networks (CNNs) to colorectal cancer histopathology is presented in [26], which proposed the Accurate, Reliable, and Active (ARA) image classification framework using a Bayesian CNN (ARA-CNN). The model integrates uncertainty estimation through variation dropout-out-based entropy to detect mislabeled samples and enhance training efficiency. It achieved a 45% faster learning rate, a classification accuracy of 92.44% under 10-fold cross-validation, and an AUC of 99.5%.

The research presented in [27] Proposed a novel feature representation approach that integrates multiple texture-based descriptors within the complex Shearlet domain. The method focuses on extracting four prominent descriptors: texture features from co-occurrence matrices, LBP, LOSIB, and segmentation-driven fractal analysis, enabling robust modeling of local and global image properties. The method leverages both the magnitude and relative phase components of Shearlet coefficients and employs Principal Component Analysis (PCA) for dimensionality reduction. Evaluated using Support Vector Machine (SVM) and Decision Tree Bagger (DTB) classifiers, the approach achieved a state-of-the-art accuracy of 92.56% on the Kather histopathological dataset.

This study [28] proposed a transfer learning-based approach that leverages multiple convolutional neural network (CNN) architectures to generate an ensemble of models. Particle Swarm Optimization (PSO) is employed to dynamically select a relevant subset of these models, which are then combined using voting or averaging strategies. Validated on a histopathological dataset with seven CNN architectures, the method achieved an accuracy of 94.52% using ResNet121 in conjunction with a voting scheme, demonstrating the effectiveness of dynamic ensembling for improving classification performance.

The research presented in [29] Developed a customized convolutional neural network (CNN) model and validated its performance on the Kather-5000 dataset. A comparative analysis involving twenty machine learning models based on manually extracted features demonstrated that the proposed CNN achieved the lowest classification error rate of 22.7%, highlighting its effectiveness over traditional approaches.

The study presented in [30] Utilized the Colorectal Histology dataset, which consists of 5,000 images collected from the University Medical Center Mannheim. The proposed approach involves two main steps: (1) Feature learning facilitated by convolutional filters within neural architectures via transfer learning, and (2) classification using various machine learning algorithms, including Bayes Multilayer, k-Nearest Neighbors, Random Forest, Naive Bayes, and Support Vector Machine (SVM). Among the 108 evaluated feature extractor–classifier combinations, the pairing of DenseNet169 with an SVM using the RBF kernel yielded the best results, achieving an accuracy of 92.08%, an F1-score of 92.117%, and maintaining a low computational cost.

The study presented in [31] Evaluated five machine learning algorithms—SVM, biologically inspired networks (ANN), proximity-based learners (KNN), probabilistic discriminants with quadratic boundaries (QDA), and hierarchical partitioning techniques (CDT)—on a dataset of 3,504 training and 1,496 testing images. The study shows that combining texture-based representations from multichannel color features improves classification performance. QDA achieved the highest accuracy, exceeding 97% on both sets, particularly with the RGB color space. This method outperforms prior approaches that rely solely on grayscale features.

The results reported in [32] Suggest that the proposed ensemble techniques using the product rule and E-CNN using majority voting—are effective for colorectal cancer histopathology classification. The framework employs fine-tuned pre-trained models with block-wise adaptation, along with added dense and dropout layers to en-

hance feature learning. The ensemble aggregation significantly improves classification performance, achieving accuracies of 95.20% on the Stoean dataset (357 images) and 94.52% on the Kather dataset (5,000 images), outperforming existing methods. As reported in [33], a hybrid deep learning framework combining a dilated ResNet-101 with an attention module for feature extraction. Neighborhood Component Analysis (NCA) is used for feature reduction, observed by classification using a Deep Support Vector Machine (DeepSVM) inside an ensemble strategy. Validated on the CRC-5000 dataset, the model achieved 98.75% accuracy, demonstrating superior efficiency and generalizability over existing methods.

In a recent study, [34] introduced a computationally efficient snapshot ensemble approach using MobileNet-V2, capturing model snapshots at different epochs to extract deep features from the final layer. Particle Swarm Optimization (PSO) is employed for dimensionality reduction, achieving a 53.75% reduction in feature space while preserving high classification performance. The method achieved state-of-the-art results on a public CRC dataset, with 97.60% accuracy and a 97.61% F1-score.

The existing literature primarily emphasizes feature extraction, ensemble learning, transfer learning, and model selection, with limited focus on systematically optimizing hyperparameters of pretrained deep learning models. Although techniques like PSO and Neighborhood Component Analysis (NCA) have been applied for feature selection and ensembling, the use of advanced hyperparameter optimization (HPO) methods remains underexplored in histopathological image classification.

To address this gap, our study explores the impact of HPO using the Manta Ray Foraging Optimization (MRFO) algorithm for pretrained models. Unlike traditional manual or heuristic-based tuning, MRFO provides a more adaptive and robust search strategy. The subsequent section outlines the core concepts and algorithms underpinning the proposed approach.

3. Materials and Methods

3.1. Dataset and Preprocessing

In this study, we utilize the Kather_Texture_2016_Image_Tiles_5000 collection of texture images [35], which consists of 5,000 high-resolution, non-overlapping image patches (150 × 150) extracted from hematoxylin and eosin (H&E)-stained colorectal cancer tissue slides. These images are categorized into eight histologically meaningful classes that reflect key components of the tumor microenvironment. The TUMOR class represents malignant epithelial regions with abnormal cell growth, while STROMA corresponds to the connective tissue framework that supports tumors. COMPLEX regions exhibit mixed or intricate structures combining tumor, stromal, and other elements. LYMPHO denotes areas of lymphocytic infiltration, highlighting the immune system's interaction with cancer cells, and DEBRIS captures necrotic or degenerated tissue resulting from cell death. The MUCOSA class represents the normal epithelial lining of the gastrointestinal tract, whereas ADIPOSE depicts fat tissue that may influence tumor progression. Finally, the EMPTY class corresponds to background regions without meaningful tissue content, often representing artifacts or slide gaps. **Figure 1** illustrates representative examples of each category.

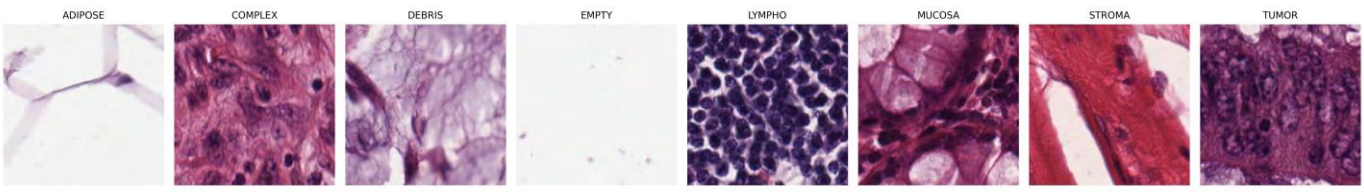

Figure 1. Randomly selected tiles from the *Kather_Texture_2016_Image_Tiles_5000* dataset showcase distinct histological patterns across eight tissue classes. Adipose and lymphoid tissues exhibit clear morphological signatures—vacuolated fat cells and dense immune nuclei, respectively. Tumor regions display pleomorphic, irregular structures, while mucosa and stroma reveal organized epithelial and fibrous frameworks. Complex and debris tiles highlight mixed and degraded tissue zones, and empty tiles represent non-informative backgrounds. This visual diversity supports robust multi-class classification in histopathology.

In fact, this dataset has been widely employed in numerous investigations, particularly in the development of deep learning algorithms for the automatic detection and classification of tissue features related to colorectal cancer. Despite being introduced in 2016, it remains one of the most used benchmarks in colorectal cancer histopathology, ensuring comparability with prior studies. Recent works [34], [36], [37] continue to adopt this dataset, underscoring its enduring relevance for evaluating both deep learning and optimization methods in CRC classification.

To address class imbalance, under-sampling was applied to ensure equal representation across all classes [38]. The dataset was randomly partitioned into training (80%), validation (10%), and test (10%) sets [39], yielding 4000, 496, and 496 images, respectively. This split ensures unbiased distribution across subsets and supports effective model training, while providing adequate data for performance evaluation and hyperparameter tuning [40]. All images were pre-processed by up-sampling to 224×224 and padded using bilinear interpolation. This resizing ensures compatibility with pre-trained CNN architectures, balancing computational efficiency and accuracy [41], while the interpolation preserves structural consistency and minimizes artifacts—aligning with standard practices in histopathological image analysis [42], [43].

3.2. Proposed methodology

The proposed method employs deep learning techniques for histopathological image classification by leveraging multiple convolutional neural network (CNN) architectures through a transfer learning framework.

In this study, transfer learning is applied in two phases to improve classification performance, utilizing three pretrained models: VGG16, ResNet50, and DenseNet121. These networks were initially trained using the ImageNet dataset, serve as robust feature extractors tailored for large-scale image classification tasks. **VGG16** is a 16-layer CNN comprising 13 convolutional and 3 fully connected layers, structured into five blocks. It employs 3×3 filters to enhance feature localization and depth while maintaining manageable complexity. Its simplicity and transfer learning efficacy make it a reliable baseline [44].

ResNet50 is a 50-layer deep CNN organized into 16 residual blocks. It uses identity shortcuts to mitigate vanishing gradients, enabling stable training of deeper networks and effective hierarchical feature extraction [45]. **DenseNet121** consists of 121 layers with dense connectivity, where each layer receives inputs from all preceding layers. This promotes feature reuse and efficient gradient flow, with four dense blocks separated by transition layers to manage dimensionality and computational cost [46]. As shown in Figure 2, the framework adopts a two-phase transfer learning approach. In Phase 1, pretrained CNNs act as fixed feature extractors by freezing all layers and replacing the original classification head with a custom fully connected (FC) layer. VGG16 includes two intermediate FC layers with ReLU and dropout; other models incorporate normalization and dropout before the final layer to improve generalization. In Phase 2, selective fine-tuning is applied by unfreezing a subset of pretrained layers based on a transfer learning (TL) ratio hyperparameter. This enables gradual adaptation to the target dataset while retaining dropout-based regularization to mitigate overfitting. To boost performance during Phase 2, the Manta Ray Foraging Optimization (MRFO) algorithm is applied to tune key hyperparameters. As detailed in Algorithm 1, MRFO efficiently searches for optimal values of optimizer type, TL ratio, dropout rate, and batch size. This guided tuning enhances model accuracy and generalization on the target dataset.

Algorithm 1: Manta Ray Foraging Optimization Deep Learning Approach (CrcMRFA)

Input: *model_names, NO_ITERATION, population, ranges*
Output: *bestSolutions, bestScores*

```
For model_name in model_names:
    Initialize bestSolutions, bestScores
    For iteration = 1 to NO_ITERATION:
        score_list ← [fitnessFunction(ind) for ind in population]
        population ← populationUpdate(population, score_list)
        Update bestSolutions and bestScores
```

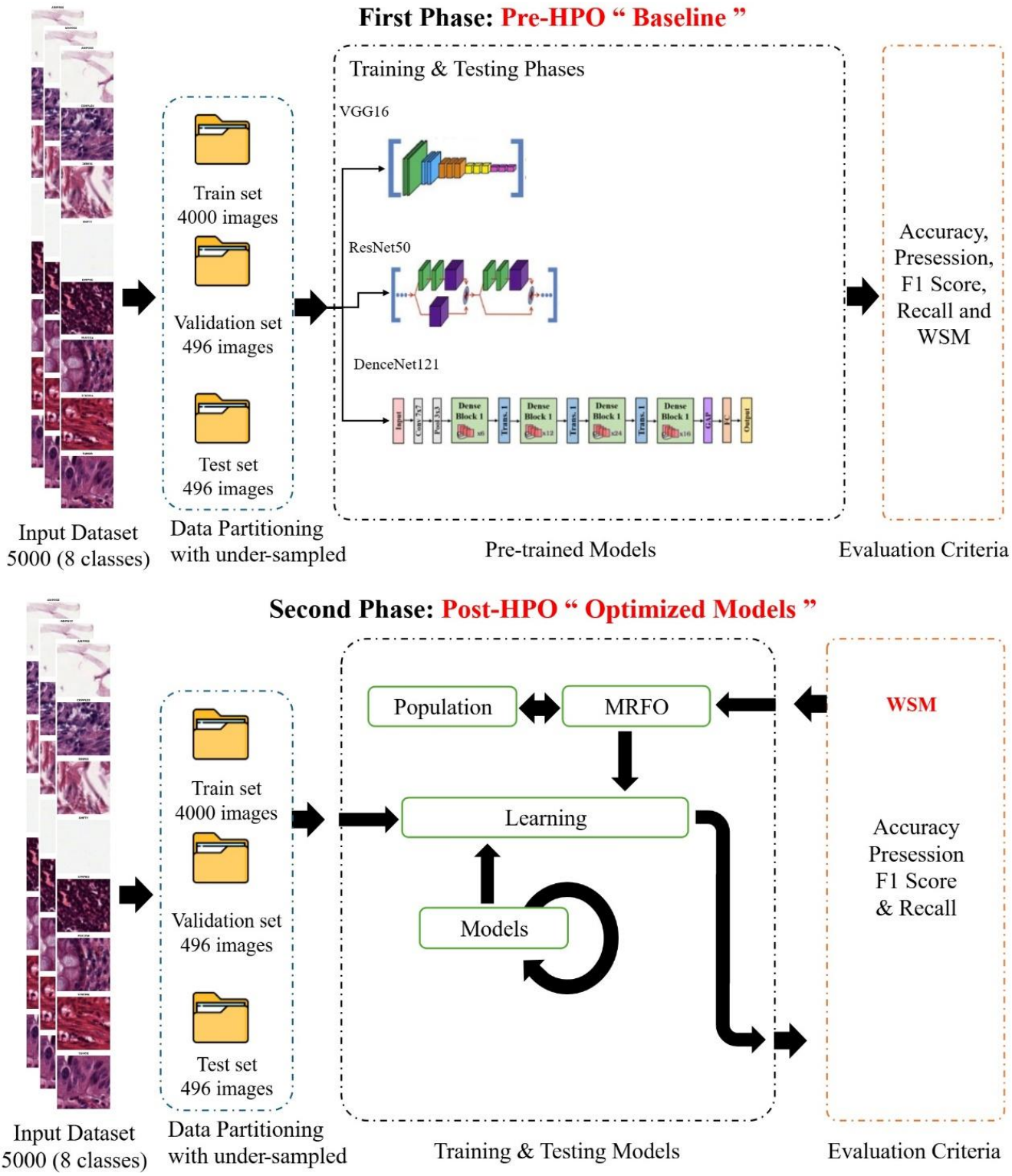

Figure 2. Graphical overview of the proposed two-phase deep learning pipeline for multi-class tissue classification. In the first phase, three pre-trained models (VGG16, ResNet50, and DenseNet121) are trained and evaluated on an under-sampled histopathological dataset (5000 images across 8 classes), establishing baseline metrics using Accuracy, Precision, Recall, F1 Score, and Weighted Scoring Metric (WSM). The second phase applies population-based hyperparameter optimization (HPO) to refine model configurations, followed by re-evaluation using the same metrics and data partitions. This abstraction highlights the performance gains achieved through systematic optimization and supports reproducible benchmarking across architectures.

Figure 3 illustrates the operational flowchart of the Manta Ray Foraging Optimization (MRFO) algorithm, outlining its key procedural steps. Intuitively, MRFO simulates the intelligent foraging strategies of manta rays, including chain foraging, cyclone foraging, and somersault foraging, which balance exploration of the search space with exploitation around promising solutions. This balance makes MRFO particularly suitable for high-dimensional medical imaging tasks, where it is essential to avoid local-minima while efficiently refining promising hyperparameter regions. The corresponding pseudocode is presented in **Algorithm 2**, which has been adapted from the original MATLAB implementation and rewritten in Python for integration into our pipeline. Unlike traditional metaheuristic optimizers such as Particle Swarm Optimization (PSO) and Genetic Algorithms (GA), which may prematurely converge or require extensive tuning, MRFO introduces dynamic movement strategies that improve population diversity and search efficiency. This distinction underlines the novelty of our approach in applying MRFO for hyperparameter optimization in colorectal cancer histopathological image classification. The original MATLAB source code is publicly available at [47].

Algorithm 2: pseudocode of the Manta Ray Foraging Optimization algorithm

Input: Population size N, maximum iterations T, bounds $[L_b, U_b]$, problem dimension D
Output: optimal solution x_{best}

Initialize population size $\{x_i\}_{i=1}^{N}$, randomly within $[L_b, U_b]$
Set iteration counter $t \leftarrow 0$
Evaluate fitness $f(x_i)$ for each manta ray
Set the initial best solution $x_{best}(t)$
While $t \le T$**:**
  For each manta ray $i = 0, \ldots\ldots, N$:
    Generate random numbers r, $r_1 \sim \cup[0,1]$
    $\beta = 2 \cdot \exp\left(r_1 \cdot \frac{T-t+1}{T}\right) \cdot \sin(2\pi r_1)$ #Cyclone Foraging
    $\alpha = 2 \cdot rand(D) \cdot \sqrt{|\ln(r)|}$ #Chain Foraging
    If $r < 0.5$**:** #Cyclone Foraging
      $c \leftarrow t / T$ # Coefficient
      If $c > r$**:**
        If i = 0**:**
          $x_i(t+1) = x_{best}(t) + (r + \beta)\,(x_{best}(t) - x_i(t))$
        Else:
          $x_i(t+1) = x_{best}(t) + \beta\,(x_{best}(t) - x_i(t)) + r\,(x_{i-1}(t) - x_i(t))$
      Else:
        If i = 0**:**
          $x_i(t+1) = x_{rand}(t) + \beta\,(x_{rand}(t) - x_i(t)) + r\,(x_{best}(t) - x_i(t))$
        Else:
          $x_i(t+1) = x_{rand}(t) + \beta\,(x_{rand}(t) - x_i(t)) + r\,(x_{i-1}(t) - x_i(t))$
    Else:
      If i = 0**:** #Chain Foraging
        $x_i(t+1) = x_i(t) + \alpha\,(x_{best}(t) - x_i(t)) + r\,(x_{best}(t) - x_i(t))$
      Else:
        $x_i(t+1) = x_i(t) + \alpha\,(x_{best}(t) - x_i(t)) + r\,(x_{i-1}(t) - x_i(t))$
    Evaluate fitness $f(x_i(t+1))$
    If $f(x_i(t+1)) > f(x_{best})$, update $x_{best} \leftarrow x_i(t+1)$
    $x_i(t+1) = x_i(t) + s \cdot (r_2 \cdot x_{best} - r_3 \cdot x_i(t))$ # Somersault Foraging
    Evaluate fitness $f(x_i(t+1))$
    If $f(x_i(t+1)) > f(x_{best})$, update $x_{best} \leftarrow x_i(t+1)$
  Increment $t \leftarrow t+1$

This structured approach, combining transfer learning and hyperparameter optimization, improves the reliability and effectiveness of deep models for histopathological image categorization in colorectal cancer staging. A loop is executed for each pretrained CNN model, following these steps:

1) Population Initialization: The initial population consists of ten solutions, each representing four hyperparameters to be optimized. This forms a (10, 4) matrix, with each value randomly initialized between 0 and 1. These values are then mapped to their respective hyperparameter ranges.

2) Calculating Fitness Scores: For each solution, fitness scores are computed as outlined in **Algorithm 3**. The solutions are mapped to their corresponding hyperparameters, which are used in training the selected pre-trained convolutional model trained for a specific number of iterations. After training, the model's Predictive capability is evaluated using five metrics: accuracy, precision, recall, F1-score, and area under the curve (AUC) for each class [48]. The results are stored in the population scores list.

Algorithm 3: Fitness Function

Input: *solution*
Output: *score*
1 Map *solution* parameters to *batch size, optimizer, TL ratio,* and *dropout*
2 Initialize data loaders for *train, validation, and tes*t with appropriate shuffling
3 Build a model with mapped hyperparameters
4 Define the loss function and *optimizer*
5 Train model and record metrics
6 Evaluate model on test set to obtain *score*

Since the dataset is balanced, **accuracy** serves as a reliable indicator of overall model performance, representing the proportion of correctly classified samples, as shown in **Equation (1)** To evaluate class-wise performance, we compute **precision**, **recall**, and **F1-score** using standard (macro or weighted) averaging.

Precision captures the extent to which predicted instances within each class are correctly identified, as shown in **Equation (2).** Recall, shown in **Equation (3),** quantifies the proportion of actual instances correctly identified by the model. Finally, the F1-score brings together how often the model is right (precision) and how often it finds all the right answers (recall), offering a fair overall score, as described in **Equation (4)**.

$$Accracy = \frac{\sum_{i=1}^{n} TP_i}{\sum_{i=1}^{n}(TP_i + FP_i + TN_i + FN_i)} \quad (1)$$

where n is the total number of classes, i is the class we are currently evaluating, TP_i is the true positives for class i (correctly predicted samples of class i), FP_i is the false positives for class i (samples incorrectly predicted as class i), TN_i is the true negatives for class i (samples not in class i that were also not predicted as i). FN_i is the false negatives for class i (samples of class i incorrectly predicted as another class).

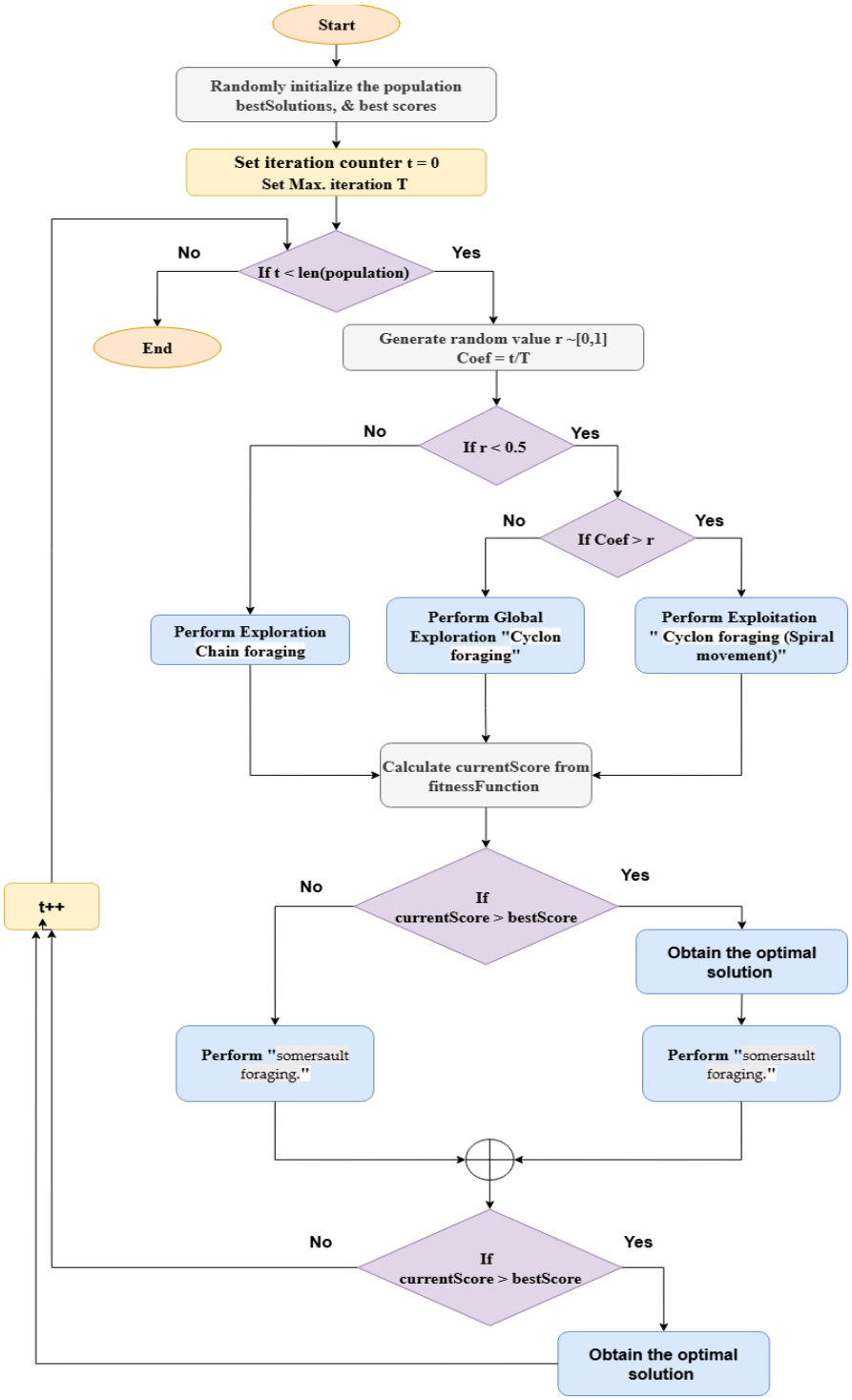

Figure 3. Flowchart illustrating the Manta Ray Foraging Optimizer (MRFO), a nature-inspired metaheuristic algorithm modeled on the foraging strategies of manta rays. The process begins with random population initialization and iteratively applies three biologically motivated behaviors: chain foraging for local exploration, cyclone foraging for global search (including spiral movement for exploitation), and somersault foraging to intensify convergence around promising solutions. Random coefficients guide behavioral transitions, and fitness evaluations update the best solution. This abstraction captures the balance between exploration and exploitation, enabling robust optimization in high-dimensional search spaces.

$$Weighted\ Precision = \sum_{i=1}^{n} \left(\frac{TP_i + FN_i}{\sum_{j=1}^{n} (TP_j + FN_j)} \times \frac{TP_i}{TP_i + FP_i} \right) \quad (2)$$

$$Weighted\ Recall = \sum_{i=1}^{n}\left(\frac{TP_i + FN_i}{\sum_{j=1}^{n}(TP_j + FN_j)} \times \frac{TP_i}{TP_i + FN_i}\right) \quad (3)$$

$$Weighted\ F1-score = \sum_{i=1}^{n}\left(\frac{TP_i + FN_i}{\sum_{j=1}^{n}(TP_j + FN_j)} \times \frac{2 \times P_i \times R_i}{P_i + R_i}\right) \quad (4)$$

Where j all classes when computing total dataset size, P_i precision for class i ($P_i = \frac{TP_i}{TP_i + FP_i}$), and R_i recall for class i ($R_i = \frac{TP_i}{TP_i + FN_i}$).

We also calculate AUC-ROC using a One-vs-Rest (OvR) strategy, which evaluates the model's capability to differentiate each class based on probability scores. These metrics provide a robust evaluation of the model's classification performance on a balanced dataset. To synthesize multiple performance indicators into one comprehensive fitness value [49], we apply the Weighted Sum Approach (WSM) [50], we assign equal weights (w_i = 0.2) are assigned to all five metrics in **Equation (5)** to ensure balanced optimization across accuracy, precision, recall, F1, and AUC. This reflects (a) the lack of clinical or modeling rationale for favoring any single metric, (b) the need to prevent dominance and promote fair evaluation, and (c) standard multi-criteria decision-making (MCDM) practice when preferences are uniform or unspecified, especially since all metrics are monotonic with "higher-is-better" behavior.

$$WSM = \sum_{i=1}^{n} w_i \times M_i,\ \ where: w_i > 0,\ \sum_{i=1}^{n} w_i = 1 \quad (5)$$

where w_i is the weight of the metric i, n is the total number of metrics and M_i value of the i^{th} evaluation metric (e.g., Accuracy, Precision, Recall, F1-score, AUC).

3) Population Updating: Once fitness values are determined, the population evolved to the next generation using the MRFO procedure discussed earlier. This process is repeated until MRFO optimization is completed.

3.3. Experimental setup

The experimental setup consists of two phases: baseline evaluation and hyperparameter optimization. The general configurations applied to both phases are summarized in **Table 1**.

Table 1. Experimental Configurations for Both Phases.

Parameter	Value
Dataset	Kather_Texture_2016_Image_Tiles_5000
Categories	TUMOR, STROMA, COMPLEX, LYMPHO, DEBRIS, MUCOSA, ADIPOSE, EMPTY
Splitting Ratio	80% (train), 10% (validation), 10% (test)
Dataset Size	5000
Preprocessing Methods	Resizing (224×224), Bilinear Interpolation
Learned Models	VGG16, ResNet50 and DenseNet121
Initialization weights	ImageNet
Output Classification Function	SoftMax
Total training cycles	60
Early Stopping Patience	3
Performance Metrics	Accuracy, Precision, F1-score, AUC, Recall
Maximum iteration Num-	15

ber	
Population Size	10
Learning Environment	Dell Precision 7920 Tower, Intel Xeon Gold 6248R CPU (3.00 GHz, 48 cores), 64 GB RAM, NVIDIA RTX A4000 (16 GB VRAM)
Programming Language	Python
Python Packages	PyTorch, NumPy, OpenCV, Pandas, Matplotlib

In the first phase, the pretrained models are evaluated using default settings. **Table 2** provides a summary of the hyperparameter settings for this phase.

Table 2. Hyperparameter Settings for the First Phase.

Parameter	Value
Optimizer	Adam
Learning Rate	Default (lr = 0.001)
Transfer Learning Strategy	Classifier layers only
Batch Size	8
Dropout Ratio	VGG16: 50%.

To enhance model performance, hyperparameter optimization is performed in the second phase. Various optimizers, learning rates, transfer learning ratios, batch sizes, and dropout rates are explored, as summarized in **Table 3.**

Table 3. Hyperparameter Ranges for the Second Phase.

Parameter	Range
Optimizers	Adam, Adafactor, Adadelta, AdamW, Nadam, Adagrad, ASGD, SGD, RMSprop
Learning Rate	Default (Adam, AdamW, and SGD (0.001), Nadam (0.002), RMSprop, Adagrad, Adafactor, and ASGD (0.01), and Adadelta (1.0))
Transfer Learning Ratios	[0:5:80]%
Batch Sizes	4, 8, 16
Dropout Ratios	[0:60]%

4. Findings and Implications

The effectiveness of MRFO was validated through a comparative analysis of baseline models and their MRFO-optimized versions.

4.1. Quantitative and Qualitative Analysis

As shown in **Table 4**, ResNet50 outperformed DenseNet121 and VGG16 in the baseline evaluation, establishing it as the most effective model for histopathological image classification. Following MRFO-based optimization in **Table 5**, all models demonstrated substantial performance gains, with ResNet50 maintaining its superiority. These results underscore the benefits of optimization in enhancing model accuracy and overall classification robustness and highlight ResNet50 as the most reliable choice for this task.

Table 4. Performance Evaluation of Baseline Models.

Model	Accuracy	Precision	Recall	F1 Score	AUC-ROC	WSM Score
DenseNet121	88.10%	88.14%	88.10%	87.95%	0.9859	90.18%

ResNet50	**90.32%**	**90.73%**	**90.32%**	**90.14%**	**0.9924**	**92.15%**
VGG16	86.29%	87.89%	86.29%	86.15%	0.9791	88.91%

Table 5. Performance Evaluation of MRFO-Optimized Models.

Model	Accuracy	Precision	Recall	F1 Score	AUC-ROC	WSM Score
DenseNet121	94.96%	95.00%	94.96%	94.93%	0.9974	95.92%
ResNet50	**95.97%**	**96.16%**	**95.97%**	**95.98%**	**0.9975**	**96.77%**
VGG16	94.96%	94.99%	94.96%	94.96%	0.9964	95.90%

These improvements validate the effectiveness of the MRFO optimization strategy in fine-tuning model hyperparameters, thereby enhancing the overall classification capability in histopathological image analysis tasks. The statistical analysis further confirmed this observation. Normality checks on the paired differences (optimized – baseline) using Shapiro–Wilk, Anderson–Darling, and in **Figure 4** the QQ-plots indicated no substantial deviation from normality, despite the small sample size (n = 3). Accordingly, the paired t-test results were considered more reliable in this setting and confirmed significant gains in Accuracy ($p = 0.015$), Precision ($p = 0.006$), Recall ($p = 0.015$), F1 score ($p = 0.014$), and WSM score ($p = 0.014$). The improvement in AUC-ROC ($p = 0.085$) was not statistically significant, likely because the baseline models already achieved very high AUC values. Although the Wilcoxon signed-rank test did not detect significance due to the limited number of paired observations, the paired t-test—appropriate under the observed normality of differences—demonstrated consistent improvements across nearly all metrics. Overall, these findings indicate that optimization significantly enhanced performance in classification-related measures, while AUC improvements remained modest given the strong baseline values.

To obtain a more comprehensive view of the **ResNet50** functionality, a confusion matrix in **Figure 5** demonstrates that the model demonstrates strong performance with notable accuracy across most classes. ADIPOSE (TP = 61) and DEBRIS (TP = 61) show perfect classification, while EMPTY (TP = 61) also performs well with only one incorrectly identified instance (FP = 1). The MUCOSA (TP = 62) class achieves flawless results. However, STROMA shows eight misclassification (FN = 8) and three missed detections (FP = 3), indicating a potential overlap with other classes like COMPLEX and DEPRIS. The counts of correctly classification (TN) remain high across all classes, suggesting that the model is effectively rejecting irrelevant categories in most cases. In the **Figure 6** The ROC curves revealed near-perfect separability, with AUC values approaching the upper bound of 1.00, underscoring the model's strong discriminative capability—even in complex categories such as TUMOR and COMPLEX. Complementing this, the PR curves exhibited high precision sustained over a wide recall range, Reflecting minimal false positives and stable accuracy in true case recognition, these metrics collectively affirm the model's robustness, sensitivity, and applicability to histopathological image classification. In clinical settings, black-box predictions are insufficient; pathologists and regulatory bodies demand transparency. Integrating explainable AI (XAI) techniques—such as class activation maps (CAMs), Grad-CAM, or attention-based visualizations—could help elucidate which histological features drive model predictions, especially in borderline cases like STROMA, where misclassifications were observed. Such insights are critical for building trust and enabling collaborative decision-making between AI systems and clinicians.

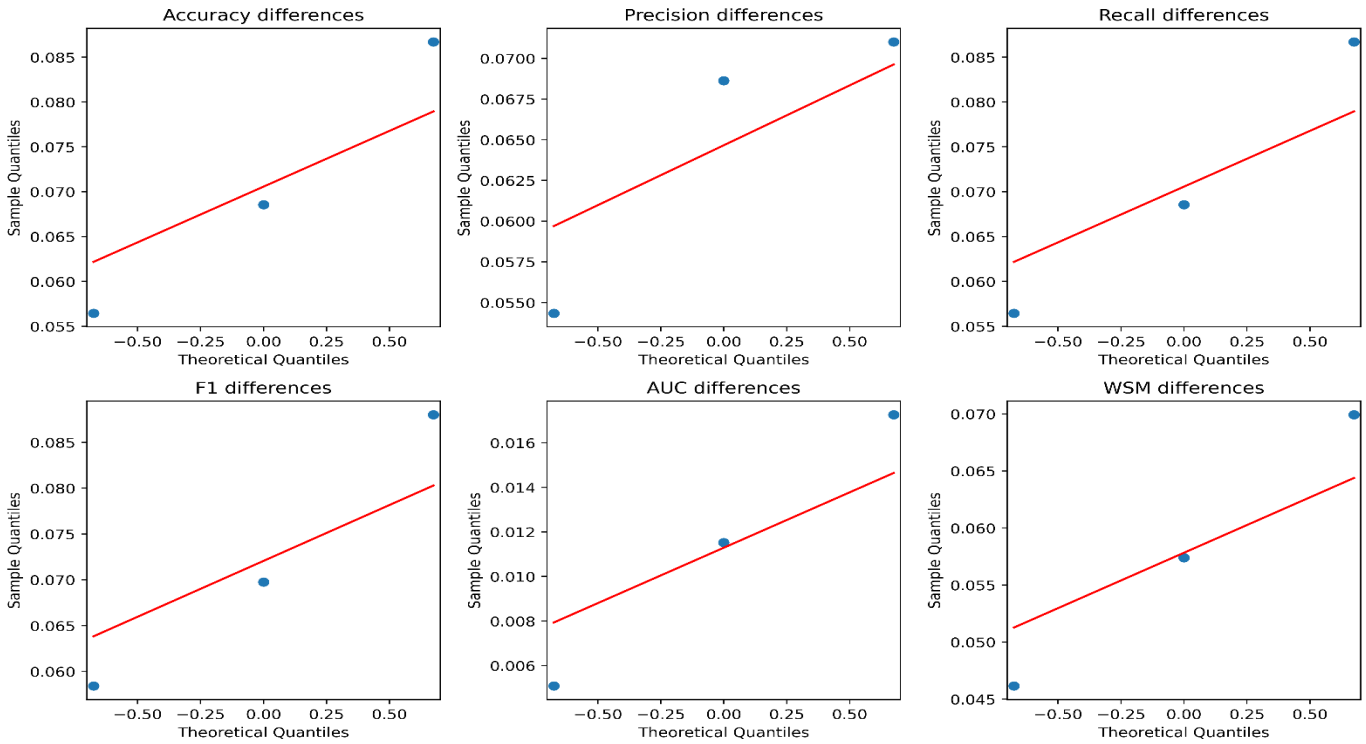

Figure 4: QQ-plots of the paired performance differences (optimized – baseline) for all evaluation metrics (Accuracy, Precision, Recall, F1 score, AUC, and WSM). The plots show that the data points largely follow the theoretical normal distribution line, indicating no substantial deviations from normality. This supports the use of the paired *t*-test for statistical comparison despite the small sample size ($n = 3$).

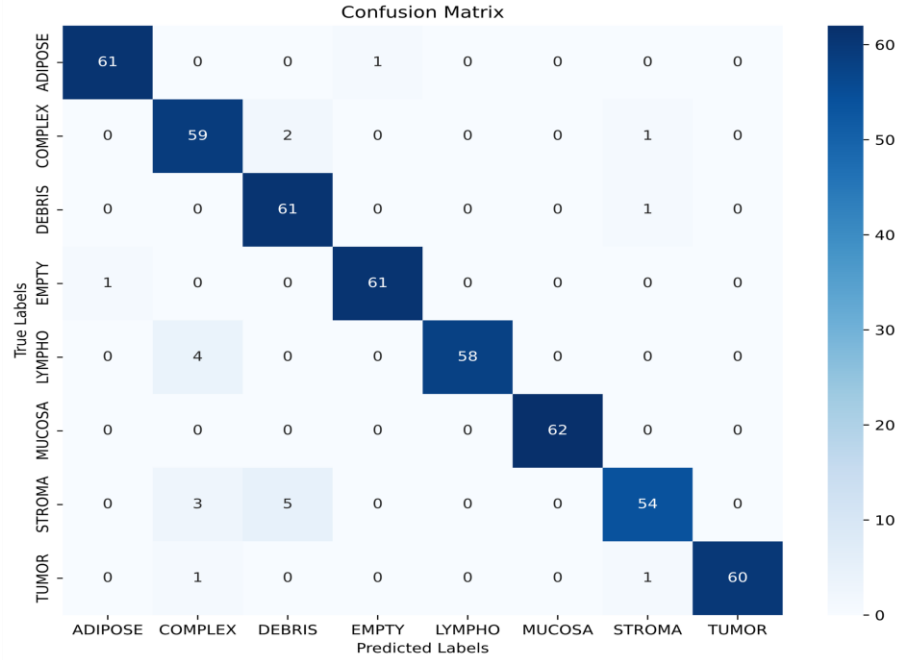

Figure 5. Confusion matrix illustrating the classification performance of the Optimized ResNet50 model across eight histological tissue classes. Strong diagonal dominance indicates high predictive accuracy, with perfect or near-perfect classification for ADIPOSE, EMPTY, MUCOSA, and TUMOR. Minor misclassifications occur primarily between structurally similar classes such as STROMA and COMPLEX, suggesting potential overlap in feature representations.

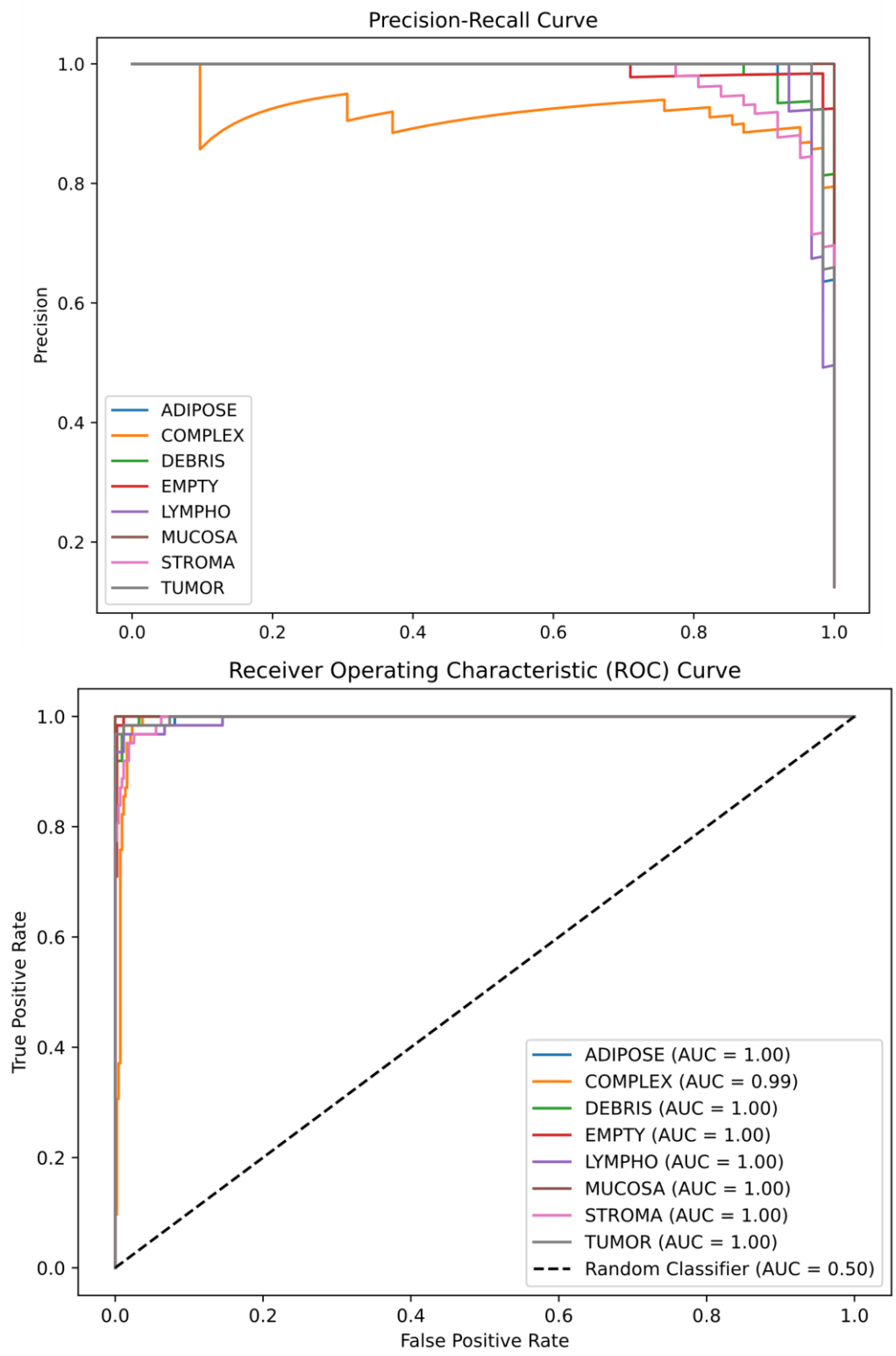

Figure 6. Performance curves for the Optimized ResNet50 model on multi-class tissue classification. Top panel: Precision-Recall curves demonstrate high discriminative power across most tissue classes, with ADIPOSE, LYMPHO, MUCOSA, STROMA, and TUMOR achieving near-perfect precision and recall. The COMPLEX class shows reduced performance, indicating classification challenges due to structural ambiguity. Lowest panel: ROC curves reveal strong sensitivity and specificity, with most classes approaching the top-left corner, signifying excellent true positive rates and minimal false positives. These curves validate the model's robustness and reliability following hyperparameter optimization.

4.2. Performance Comparison with Advanced Models

Table 6 Presents a performance-oriented comparison between the introdced method relative to contemporary advanced techniques on the Kather_texture_2016_image_tiles_5000 dataset, ranked by accuracy in descending order. The results demonstrate that the proposed method outperforms all others, achieving the highest values across four evaluation metrics and ranking second in F1-score.

Table 6. Performance Comparison with Advanced Models

Ref.	Method	Feature Extraction + Classifier	Accuracy	Precision	Recall	F1 Score	AUC-ROC
[51]	ML	LPQ + BSIF + NN	74.22%	-	-	-	-
[32]	DL	E-CNN (DenseNet121, MobileNetV2, InceptionV3, and VGG16) – Product Fusion	91.28%	-	79.97%	-	-
[30]	Hybrid	DenseNet169 + SVM (RBF)	92.08%	-	-	92.12%	-
[26]	DL	ARA-CNN	92.44%	-	-	-	**0.995**
[27]	ML	Fusion of CM, LBP, LOSIB, SFTA, and CM dot + SVM	92.54%	92.67%	92.54%	-	0.9906
[52]	DL	Ensemble weights (DenseNet121, InceptionResNetV2, Xception, + custom CNN)	92.83%	92.83%	93.11%	**96.16%**	0.9616
[53]	DL	Customized CNN model	93.50%	**94.12%**	93.62%	93.86%	0.9573
[31]	ML	Haralick features using 3D co-occurrence matrices in LAB color space + QDA	94.04%	-	**94.00%**	-	-
[28]	DL	Modified ResNet121 with added layers + PSO for model selection + voting	94.52%	-	-	-	-
[54]	ML	WPT, Gabor filters, LBP, GLCM, FOS & HOS + ANOVA test + ANN	95.32%	-	-	-	-
[55]	Hybrid	VGG19 + NN	**95.46%**	-	-	94.00%	-
Proposed Method	Optimized DL	**CrcMRFA (ResNet50)**	**95.97%**	**96.16%**	**95.97%**	**95.98%**	**0.9975**

4.3. Study limitations

This study has several limitations. First, the dataset size is minor compared to large-scale medical imaging benchmarks, which may restrict the full learning capacity of deep models. Second, only a single dataset (Kather_2016) was employed, limiting the diversity of tissue variations captured. Third, the absence of external validation across independent datasets or clinical centers constrains the assessment of generalizability. Fourth, the statistical analysis was based on only three paired backbone models (DenseNet121, ResNet50, and VGG16), which reduced the power of non-parametric tests such as the Wilcoxon signed-rank test. Nevertheless, normality checks supported the use of paired *t*-tests, which confirmed significant improvements across most metrics. Future work will focus on validating the proposed approach on multi-center datasets and expanding the set of backbone models to further confirm robustness and clinical applicability.

5. Conclusions

This research highlights the effectiveness of integrating Manta Ray Foraging Optimization (MRFO) with the classification of histopathological data that is advanced using convolutional neural networks. The significant performance gains—particularly the 95.97% accuracy and 96.77% WSM score achieved by MRFO-optimized ResNet50—underscore the impact of bio-inspired optimization on medical image analysis. These results affirm the proposed framework's ability to extract rich, discriminative features while maintaining computational efficiency, which is critical for practical diagnostic use.

The proposed approach holds promise for deployment in **computer-aided diagnosis (CAD) systems**, **digital pathology workflows**, and **automated screening platforms**, where accurate and scalable image interpretation is essential. It can assist pathologists by reducing workload, improving consistency, and accelerating diagnosis, especially in resource-constrained settings.

Building on the identified limitations, future work will focus on evaluating model generalizability across larger and more diverse multi-source datasets, with particular emphasis on external validation across independent cohorts and clinical centers. To address the constraint of limited backbone models and statistical power, the study will be expanded to include a broader range of architectures, enabling more robust comparative analysis. Furthermore, incorporating domain adaptation strategies will help mitigate dataset-specific biases, while the integration of advanced mechanisms such as attention modules, transformer-based architectures, or hybrid fusion frameworks may enhance both interpretability and classification precision. Finally, the development of lightweight model variants will be explored to support real-time implementation on edge devices, thereby facilitating practical clinical adoption.

Data Availability Statement: The 'Kather_texture_2016_image_tiles_5000' dataset used in this work is open and available at https://zenodo.org/records/53169.

Conflicts of Interest: The authors state that they hold no financial stakes or private ties that may have affected the integrity of this work.

References

[1] National Cancer Institute, " What is Cancer?," National Cancer Institute. Accessed: Mar. 13, 2025. [Online]. Available: https://www.cancer.gov/about-cancer/understanding/what-is-cancer

[2] American Cancer Society, " What is colorectal cancer?," American Cancer Society. Accessed: Mar. 13, 2025. [Online]. Available: https://www.cancer.org/cancer/types/colon-rectal-cancer/about/what-is-colorectal-cancer.html

[3] World Health Organization, "Cancer," World Health Organization. Accessed: Mar. 13, 2025. [Online]. Available: https://www.who.int/news-room/fact-sheets/detail/cancer

[4] Y. Xi and P. Xu, "Global colorectal cancer burden in 2020 and projections to 2040," *Transl Oncol*, vol. 14, no. 10, p. 101174, Oct. 2021, doi: 10.1016/J.TRANON.2021.101174.

[5] U. Ladabaum, J. A. Dominitz, C. Kahi, and R. E. Schoen, "Strategies for Colorectal Cancer Screening," *Gastroenterology*, vol. 158, no. 2, pp. 418–432, Jan. 2020, doi: 10.1053/J.GASTRO.2019.06.043.

[6] R. Kumar, R. Srivastava, and S. Srivastava, "Detection and Classification of Cancer from Microscopic Biopsy Images Using Clinically Significant and Biologically Interpretable Features," *J Med Eng*, vol. 2015, pp. 1–14, Aug. 2015, doi: 10.1155/2015/457906.

[7] T. Mezei, M. Kolcsár, A. Joó, and S. Gurzu, "Image Analysis in Histopathology and Cytopathology: From Early Days to Current Perspectives," *Journal of Imaging 2024, Vol. 10, Page 252*, vol. 10, no. 10, p. 252, Oct. 2024, doi: 10.3390/JIMAGING10100252.

[8] S. A. Alowais *et al.*, "Revolutionizing healthcare: the role of artificial intelligence in clinical practice," *BMC Medical Education 2023 23:1*, vol. 23, no. 1, pp. 1–15, Sep. 2023, doi: 10.1186/S12909-023-04698-Z.

[9] M. A. Abdou, "Literature review: efficient deep neural networks techniques for medical image analysis," *Neural Comput Appl*, vol. 34, no. 8, pp. 5791–5812, Apr. 2022, doi: 10.1007/S00521-022-06960-9/TABLES/5.

[10] M. Shafiq and Z. Gu, "Deep Residual Learning for Image Recognition: A Survey," *Applied Sciences 2022, Vol. 12, Page 8972*, vol. 12, no. 18, p. 8972, Sep. 2022, doi: 10.3390/APP12188972.

[11] M. Strzelecki, M. Kociołek, M. Strąkowska, M. Kozłowski, A. Grzybowski, and P. M. Szczypiński, "Artificial intelligence in the detection of skin cancer: State of the art," *Clin Dermatol*, vol. 42, no. 3, pp. 280–295, May 2024, doi: 10.1016/J.CLINDERMATOL.2023.12.022.

[12] M. N. Hamza, S. Koziel, and A. Pietrenko-Dabrowska, "Design and experimental validation of a metamaterial-based sensor for microwave imaging in breast, lung, and brain cancer detection," *Scientific Reports 2024 14:1*, vol. 14, no. 1, pp. 1–17, Jul. 2024, doi: 10.1038/s41598-024-67103-9.

[13] H. Shaheen, K. Ravikumar, N. Lakshmipathi Anantha, A. Uma Shankar Kumar, N. Jayapandian, and S. Kirubakaran, "An efficient classification of cirrhosis liver disease using hybrid convolutional neural network-capsule network," *Biomed Signal Process Control*, vol. 80, p. 104152, Feb. 2023, doi: 10.1016/J.BSPC.2022.104152.

[14] A. Sahu, P. K. Das, and S. Meher, "An efficient deep learning scheme to detect breast cancer using mammogram and ultrasound breast images," *Biomed Signal Process Control*, vol. 87, p. 105377, Jan. 2024, doi: 10.1016/J.BSPC.2023.105377.

[15] M. Sharkas and O. Attallah, "Color-CADx: a deep learning approach for colorectal cancer classification through triple convolutional neural networks and discrete cosine transform," *Sci Rep*, vol. 14, no. 1, pp. 1–23, Dec. 2024, doi: 10.1038/S41598-024-56820-W;SUBJMETA=166,308,631,639,67,692;KWRD=CANCER,ENGINEERING,MEDICAL+RESEARCH.

[16] K. Rajwar, K. Deep, and S. Das, "An exhaustive review of the metaheuristic algorithms for search and optimization: taxonomy, applications, and open challenges," *Artif Intell Rev*, vol. 56, no. 11, pp. 13187–13257, Nov. 2023, doi: 10.1007/S10462-023-10470-Y/TABLES/3.

[17] P. Thapar, M. Rakhra, M. Alsaadi, A. Quraishi, A. Deka, and J. V. Naga Ramesh, "A hybrid Grasshopper optimization algorithm for skin lesion segmentation and melanoma classification using deep learning," *Healthcare Analytics*, vol. 5, p. 100326, Jun. 2024, doi: 10.1016/J.HEALTH.2024.100326.

[18] E. Alabdulkreem, M. K. Saeed, S. S. Alotaibi, R. Allafi, A. Mohamed, and M. A. Hamza, "Bone Cancer Detection and Classification Using Owl Search Algorithm With Deep Learning on X-Ray Images," *IEEE Access*, vol. 11, pp. 109095–109103, 2023, doi: 10.1109/ACCESS.2023.3319293.

[19] A. A. A. A. Habeb, N. Zhu, M. M. Taresh, and T. A. A. Ali, "Deep ocular tumor classification model using cuckoo search algorithm and Caputo fractional gradient descent," *PeerJ Comput Sci*, vol. 10, p. e1923, Mar. 2024, doi: 10.7717/PEERJ-CS.1923/SUPP-1.

[20] A. Majid, M. A. Alrasheedi, A. A. Alharbi, J. Allohibi, and S. W. Lee, "Modified Whale Optimization Algorithm for Multiclass Skin Cancer Classification," *Mathematics 2025, Vol. 13, Page 929*, vol. 13, no. 6, p. 929, Mar. 2025, doi: 10.3390/MATH13060929.

[21] D. Umamaheswari, M. Kannan, I. P. S. Mary, D. J. Rozario, P. M. Savitha, and B. Manimekala, "LSTM-MGTO: a novel early breast cancer detection using long short term memory based modified gorilla troops optimization algorithm," *Network Modeling Analysis in Health Informatics and Bioinformatics*, vol. 14, no. 1, pp. 1–17, Dec. 2025, doi: 10.1007/S13721-025-00509-1/METRICS.

[22] H. M. Al-Jawahry, E. S. Challaraj Emmanuel, B. Rajasekhar, R. Padmavathy, and N. Sasirekha, "Gastrointestinal Disease Classification using Mayfly Optimization Algorithm based Deep Belief Network," *2024 1st International Conference on Software, Systems and Information Technology, SSITCON 2024*, 2024, doi: 10.1109/SSITCON62437.2024.10797008.

[23] W. Zhao, Z. Zhang, and L. Wang, "Manta ray foraging optimization: An effective bio-inspired optimizer for engineering applications," *Eng Appl Artif Intell*, vol. 87, p. 103300, Jan. 2020, doi: 10.1016/J.ENGAPPAI.2019.103300.

[24] S. U. R. Khan, S. Asif, M. Zhao, W. Zou, and Y. Li, "Optimize brain tumor multiclass classification with manta ray foraging and improved residual block techniques," *Multimed Syst*, vol. 31, no. 1, pp. 1–27, Feb. 2025, doi: 10.1007/S00530-025-01670-3/METRICS.

[25] S. Adamu *et al.*, "Unleashing the power of Manta Rays Foraging Optimizer: A novel approach for hyper-parameter optimization in skin cancer classification," *Biomed Signal Process Control*, vol. 99, p. 106855, Jan. 2025, doi: 10.1016/J.BSPC.2024.106855.

[26] Ł. Rączkowski, M. Możejko, J. Zambonelli, and E. Szczurek, "ARA: accurate, reliable and active histopathological image classification framework with Bayesian deep learning," *Sci Rep*, vol. 9, no. 1, Dec. 2019, doi: 10.1038/s41598-019-50587-1.

[27] S. Alinsaif and J. Lang, "Texture features in the Shearlet domain for histopathological image classification," *BMC Med Inform Decis Mak*, vol. 20, Dec. 2020, doi: 10.1186/s12911-020-01327-3.

[28] N. Dif and Z. Elberrichi, "A new deep learning model selection method for colorectal cancer classification," *International Journal of Swarm Intelligence Research*, vol. 11, no. 3, pp. 72–88, Jul. 2020, doi: 10.4018/IJSIR.2020070105.

[29] V. Rachapudi and G. Lavanya Devi, "Improved convolutional neural network based histopathological image classification," *Evol Intell*, vol. 14, no. 3, pp. 1337–1343, Sep. 2021, doi: 10.1007/s12065-020-00367-y.

[30] E. F. Ohata, J. V. S. das Chagas, G. M. Bezerra, M. M. Hassan, V. H. C. de Albuquerque, and P. P. R. Filho, "A novel transfer learning approach for the classification of histological images of colorectal cancer," *Journal of Supercomputing*, vol. 77, no. 9, pp. 9494–9519, Sep. 2021, doi: 10.1007/s11227-020-03575-6.

[31] A. M. Alqudah and A. Alqudah, "Improving machine learning recognition of colorectal cancer using 3D GLCM applied to different color spaces," *Multimed Tools Appl*, vol. 81, no. 8, pp. 10839–10860, Mar. 2022, doi: 10.1007/s11042-022-11946-9.

[32] D. Albashish, "Ensemble of adapted convolutional neural networks (CNN) methods for classifying colon histopathological images," *PeerJ Comput Sci*, vol. 8, 2022, doi: 10.7717/peerj-cs.1031.

[33] M. Khazaee Fadafen and K. Rezaee, "Ensemble-based multi-tissue classification approach of colorectal cancer histology images using a novel hybrid deep learning framework," *Sci Rep*, vol. 13, no. 1, Dec. 2023, doi: 10.1038/s41598-023-35431-x.

[34] S. Chattopadhyay, P. K. Singh, M. F. Ijaz, S. K. Kim, and R. Sarkar, "SnapEnsemFS: a snapshot ensembling-based deep feature selection model for colorectal cancer histological analysis," *Sci Rep*, vol. 13, no. 1, Dec. 2023, doi: 10.1038/s41598-023-36921-8.

[35] J. N. Kather *et al.*, "Multi-class texture analysis in colorectal cancer histology," *Sci Rep*, vol. 6, Jun. 2016, doi: 10.1038/srep27988.

[36] R. Elshamy, O. Abu-Elnasr, M. Elhoseny, and S. Elmougy, "Enhancing colorectal cancer histology diagnosis using modified deep neural networks optimizer," *Sci Rep*, vol. 14, no. 1, pp. 1–19, Dec. 2024, doi: 10.1038/S41598-024-69193-X;SUBJMETA=1042,117,639,705;KWRD=COMPUTATIONAL+SCIENCE,COMPUTER+SCIENCE.

[37] A. Bozdag *et al.*, "Early detection of colorectal cancer using a hybrid model with enhanced image quality and optimized classification," *Phys Eng Sci Med*, pp. 1–11, Aug. 2025, doi: 10.1007/S13246-025-01617-Y/METRICS.

[38] M. Owusu-Adjei, J. Ben Hayfron-Acquah, T. Frimpong, and G. Abdul-Salaam, "Imbalanced class distribution and performance evaluation metrics: A systematic review of prediction accuracy for determining model performance in healthcare systems," *PLOS digital health*, vol. 2, no. 11, p. e0000290, Nov. 2023, doi: 10.1371/JOURNAL.PDIG.0000290.

[39] A. Ben Atitallah, J. Kamoun, M. D. Alanazi, T. M. Alanazi, M. Albekairi, and K. Kaaniche, "An Advanced Medical Diagnosis of Breast Cancer Histopathology Using Convolutional Neural Networks," *Computers, Materials and Continua*, vol. 83, no. 3, pp. 5761–5779, May 2025, doi: 10.32604/CMC.2025.063634.

[40] O. A. Montesinos López, A. Montesinos López, and J. Crossa, "Overfitting, Model Tuning, and Evaluation of Prediction Performance," *Multivariate Statistical Machine Learning Methods for Genomic Prediction*, pp. 109–139, 2022, doi: 10.1007/978-3-030-89010-0_4.

[41] T. B. Nguyen-Tat, T. Q. Hung, P. T. Nam, and V. M. Ngo, "Evaluating pre-processing and deep learning methods in medical imaging: Combined effectiveness across multiple modalities," *Alexandria Engineering Journal*, vol. 119, pp. 558–586, Apr. 2025, doi: 10.1016/J.AEJ.2025.01.090.

[42] T. Imtiaz, S. A. Fattah, and M. Saquib, "ConDANet: Contourlet Driven Attention Network for Automatic Nuclei Segmentation in Histopathology Images," *IEEE Access*, vol. 11, pp. 129321–129330, 2023, doi: 10.1109/ACCESS.2023.3321799.

[43] S. Khalil *et al.*, "Enhancing Ductal Carcinoma Classification Using Transfer Learning with 3D U-Net Models in Breast Cancer Imaging," *Applied Sciences 2023, Vol. 13, Page 4255*, vol. 13, no. 7, p. 4255, Mar. 2023, doi: 10.3390/APP13074255.

[44] K. Simonyan and A. Zisserman, "Very Deep Convolutional Networks for Large-Scale Image Recognition," *3rd International Conference on Learning Representations, ICLR 2015 - Conference Track Proceedings*, Sep. 2014, Accessed: Jan. 28, 2025. [Online]. Available: https://arxiv.org/abs/1409.1556v6

[45] K. He, X. Zhang, S. Ren, and J. Sun, "Deep Residual Learning for Image Recognition," *Proceedings of the IEEE Computer Society Conference on Computer Vision and Pattern Recognition*, vol. 2016-December, pp. 770–778, Dec. 2015, doi: 10.1109/CVPR.2016.90.

[46] G. Huang, Z. Liu, L. Van Der Maaten, and K. Q. Weinberger, "Densely Connected Convolutional Networks," *Proceedings - 30th IEEE Conference on Computer Vision and Pattern Recognition, CVPR 2017*, vol. 2017-January, pp. 2261–2269, Aug. 2016, doi: 10.1109/CVPR.2017.243.

[47] Z. Z. and L. W. W. Zhao, "Manta ray foraging optimization (MRFO)," MathWorks. Accessed: Aug. 23, 2025. [Online]. Available: https://www.mathworks.com/matlabcentral/fileexchange/73130-manta-ray-foraging-optimization-mrfo

[48] L. Zhou *et al.*, "FPA-based weighted average ensemble of deep learning models for classification of lung cancer using CT scan images," *Sci Rep*, vol. 15, no. 1, pp. 1–19, Dec. 2025, doi: 10.1038/S41598-025-02015-W;SUBJMETA=166,639,705;KWRD=ENGINEERING,MATHEMATICS+AND+COMPUTING.

[49] C. B. Kalayci, O. Ertenlice, and M. A. Akbay, "A comprehensive review of deterministic models and applications for mean-variance portfolio optimization," *Expert Syst Appl*, vol. 125, pp. 345–368, Jul. 2019, doi: 10.1016/J.ESWA.2019.02.011.

[50] H. M. Balaha, E. M. El-Gendy, and M. M. Saafan, "CovH2SD: A COVID-19 detection approach based on Harris Hawks Optimization and stacked deep learning," *Expert Syst Appl*, vol. 186, p. 115805, Dec. 2021, doi: 10.1016/J.ESWA.2021.115805.

[51] E. Paladini, E. Vantaggiato, F. Bougourzi, C. Distante, A. Hadid, and A. Taleb-Ahmed, "Two Ensemble-CNN Approaches for Colorectal Cancer Tissue Type Classification," *J Imaging*, vol. 7, no. 3, Mar. 2021, doi: 10.3390/jimaging7030051.

[52] S. Ghosh, A. Bandyopadhyay, S. Sahay, R. Ghosh, I. Kundu, and K. C. Santosh, "Colorectal Histology Tumor Detection Using Ensemble Deep Neural Network," *Eng Appl Artif Intell*, vol. 100, Apr. 2021, doi: 10.1016/j.engappai.2021.104202.

[53] A. Kumar, A. Vishwakarma, and V. Bajaj, "CRCCN-Net: Automated framework for classification of colorectal tissue using histopathological images," *Biomed Signal Process Control*, vol. 79, Jan. 2023, doi: 10.1016/j.bspc.2022.104172.

[54] E. Trivizakis, G. S. Ioannidis, I. Souglakos, A. H. Karantanas, M. Tzardi, and K. Marias, "A neural pathomics framework for classifying colorectal cancer histopathology images based on wavelet multi-scale texture analysis," *Sci Rep*, vol. 11, no. 1, Dec. 2021, doi: 10.1038/s41598-021-94781-6.

[55] A. B. Bakht, S. Javed, H. Almarzouqi, A. Khandoker, and N. Werghi, "Colorectal cancer tissue classification using semi-supervised hypergraph convolutional network," in *Proceedings - International Symposium on Biomedical Imaging*, IEEE Computer Society, Apr. 2021, pp. 1306–1309. doi: 10.1109/ISBI48211.2021.9434036.